



















ODIN: Strong Clustering of Protoclusters at Cosmic Noon

VANDANA RAMAKRISHNAN ¹, KYOUNG-SOO LEE ¹, NICOLE FIRESTONE ², ERIC GAWISER ²,
MARIA CELESTE ARTALE ³, CARYL GRONWALL ^{4,5}, LUCIA GUAITA ³, SANG HYEOK IM ⁶, WOONG-SEOB JEONG ⁷,
SEONGJAE KIM ⁷, ANKIT KUMAR ³, JAEHYUN LEE ⁷, BYEONGHA MOON ⁷, NELSON PADILLA ⁸,
CHANGBOM PARK ⁹, HYUNMI SONG ¹⁰, PAULINA TRONCOSO ¹¹ AND YUJIN YANG ⁷

¹*Department of Physics and Astronomy, Purdue University, 525 Northwestern Avenue, West Lafayette, IN 47907, USA*

²*Physics and Astronomy Department, Rutgers, The State University, Piscataway, NJ 08854*

³*Departamento de Ciencias Físicas, Universidad Andres Bello, Fernandez Concha 700, Las Condes, Santiago, Chile*

⁴*Department of Astronomy & Astrophysics, The Pennsylvania State University, University Park, PA 16802, USA*

⁵*Institute for Gravitation and the Cosmos, The Pennsylvania State University, University Park, PA 16802, USA*

⁶*Department of Physics and Astronomy, Seoul National University, 1 Gwanak-ro, Gwanak-gu, Seoul 08826, Republic of Korea*

⁷*Korea Astronomy and Space Science Institute, 776 Daedeokdae-ro, Yuseong-gu, Daejeon 34055, Republic of Korea*

⁸*Instituto de Astronomía Teórica y Experimental (IATE), CONICET-UNC, Laprida 854, X500BGR, Córdoba, Argentina*

⁹*Korea Institute for Advanced Study, 85 Hoegi-ro, Dongdaemun-gu, Seoul 02455, Republic of Korea*

¹⁰*Department of Astronomy and Space Science, Chungnam National University, 99 Daehak-ro, Yuseong-gu, Daejeon, 34134, Republic of Korea*

¹¹*Escuela de Ingeniería, Universidad Central de Chile, Avenida Francisco de Aguirre 0405, 171-0614 La Serena, Coquimbo, Chile*

ABSTRACT

The One-hundred-deg² DECam Imaging in Narrowbands (ODIN) survey is carrying out a systematic search for protoclusters during Cosmic Noon, using Ly α -emitting galaxies (LAEs) as tracers. Once completed, ODIN aims to identify hundreds of protoclusters at redshifts of 2.4, 3.1, and 4.5 across seven extragalactic fields, covering a total area of up to 91 deg². In this work, we report strong clustering of high-redshift protoclusters through the protocluster-LAE cross-correlation function measurements of 150 protocluster candidates at $z = 2.4$ and 3.1, identified in two ODIN fields with a total area of 13.9 deg². At $z = 2.4$ and 3.1, respectively, the inferred protocluster biases are $6.6_{-1.1}^{+1.3}$ and $6.1_{-1.1}^{+1.3}$, corresponding to mean halo masses of $\log\langle M/M_{\odot} \rangle = 13.53_{-0.24}^{+0.21}$ and $12.96_{-0.33}^{+0.28}$. By the present day, these protoclusters are expected to evolve into virialized galaxy clusters with a mean mass of $\sim 10^{14.5} M_{\odot}$. By comparing the observed number density of protoclusters to that of halos with the measured clustering strength, we find that our sample is highly complete. Finally, the similar descendant masses derived for our samples at $z = 2.4$ and 3.1 assuming that the halo number density remains constant suggest that they represent similar structures observed at different cosmic epochs. As a consequence, any observed differences between the two samples can be understood as redshift evolution. The ODIN protocluster samples will thus provide valuable insights into the cosmic evolution of cluster galaxies.

1. INTRODUCTION

The effect of environment on the formation and evolution of galaxies is a question of considerable importance. In the local Universe, clusters of galaxies display an excess of massive and quiescent galaxies compared to the coeval field (e.g., Peng et al. 2010; Quadri et al. 2012). These galaxies are expected to have assembled the bulk of their mass at high redshifts ($z \sim 2 - 4$). Indeed at $z \gtrsim 2$, the progenitors of present-day clusters of galaxies (‘protoclusters’) host copious star-formation and AGN activity (e.g., Casey et al. 2015; Oteo et al. 2018; Harikane et al. 2019; Staab et al. 2024) as well as

evolved galaxies (Ito et al. 2023; Jin et al. 2024), suggesting ongoing rapid mass assembly. Thus, in order to understand the growth of galaxies in overdense regions, it is necessary to study protoclusters.

In recent years, studies have begun identifying increasingly large samples of protoclusters through various methods (e.g., Chiang et al. 2014; Toshikawa et al. 2016, 2018; Higuchi et al. 2019). Yet, connecting these objects with clusters identified at lower redshifts remains challenging. This is in large part because protoclusters remain unvirialized and lack several of the characteristics of clusters such as a red sequence or hot intra-cluster medium (see Overzier 2016, for a review). As they are

observed in the initial phases of their formation, it is difficult to determine what characteristics they may ultimately exhibit.

One of the protocluster properties most useful for judging their evolution is the halo mass, as we expect that the halo mass of the most massive halo within a protocluster is indicative of the mass of the final cluster (Chiang et al. 2013). One way to determine the halo mass is through measurements of the clustering strength of the protoclusters, as more massive halos are also more strongly clustered (Sheth & Tormen 1999). However, such measurements require a large sample to carry out, which has prevented them from being widely used so far.

Recently, we presented the selection of protoclusters from the One-hundred-deg² DECam Imaging in Narrowbands (ODIN, Lee et al. 2024) survey in Ramakrishnan et al. (2024). By imaging a wide area of the sky with three custom narrowband filters, ODIN has made it possible to identify a large and robust protocluster sample at Cosmic Noon. In this work, we explore the clustering of ODIN protoclusters selected at $z = 2.4$ and 3.1. In Section 2, we present our protocluster sample. We analyze the clustering using the two-point correlation function in Section 3. We interpret our results for the halo mass and probable descendants of the ODIN structures in Section 4. Finally, we summarize our findings in Section 5. Throughout, we assume a Planck cosmology (Planck Collaboration et al. 2016) with $\Omega_\Lambda = 0.6911$, $\Omega_b = 0.0486$, $\Omega_m = 0.3089$, $H_0 = 100 h \text{ km s}^{-1} \text{ Mpc}^{-1}$ and $h = 0.6774$. Distances are given in comoving units, with an implicit h_{68}^{-1} .

2. PROTOCLUSTER SAMPLES

The ODIN survey is a wide-field imaging survey spanning 91 deg² of the equatorial and southern skies, utilizing three narrow-band filters— $N419$, $N501$, and $N673$ —designed to detect Ly α emission at redshifts $z = 2.4$, 3.1, and 4.5, respectively. As described in the ODIN survey paper (Lee et al. 2024), one of its primary objectives is to map large-scale structures using Ly α -emitting galaxies (LAEs), a subset of low-mass, star-forming galaxies (e.g., Gawiser et al. 2006; Guaita et al. 2010). Previous angular clustering measurements suggest that LAEs reside in moderate-mass halos with low bias (e.g., Gawiser et al. 2007; Guaita et al. 2010; Lee et al. 2014; Kusakabe et al. 2018; Hong et al. 2019; White et al. 2024).

The photometric selection of ODIN LAEs combines the ODIN narrow-band (NB) imaging data with deep broad-band imaging from the Hyper Suprime-Cam

Subaru Strategic Program (HSC-SSP; Aihara et al. 2018a,b). The selection method is detailed in Firestone et al. (2024) and is summarized as follows: (i) LAEs must be detected in the NB image with a signal-to-noise ratio of at least 5, and (ii) they must exhibit excess flux in the NB compared to the estimated continuum flux density near the Ly α wavelength. The NB-to-BB color cut corresponds to a rest-frame equivalent width of 20 Å. Sources near bright stars are excluded using HSC-SSP star masks (Coupon et al. 2018). The effective area of each field, after excluding the star-masked regions, and the number of detected LAEs are provided in Table 1.

The selection method for the protoclusters and the expected contamination rate are detailed in Ramakrishnan et al. (2024). Briefly, protoclusters are identified from maps of the LAE surface density ($1 + \delta_{\text{LAE}}$) as contiguous regions that exceed predefined thresholds in both density and angular size (A). These criteria are optimized to minimize false detections while maximizing the total number of protoclusters. We follow the procedure described in Ramakrishnan et al. (2024) to estimate the contamination rate and adopt the threshold of $\delta_{\text{LAE}} = 2.3$ (2.6), corresponding to a significance of 4σ (4.5σ) above the field surface density, for our protocluster selection at $z = 2.4$ (3.1). The lower detection threshold for the $z = 2.4$ sample is possible because of the higher LAE number density at that redshift. For both redshifts, the minimum area is chosen to be $A = 40 \text{ cMpc}^2$.

A potential concern in ensuring the robustness of our protocluster detection is the variation in imaging sensitivity across the narrow-band data used for LAE selection. ODIN employs DECam, which covers a circular area of 2.1° in diameter, to image a larger field matching the LSST field of view (FOV) of 3.5°. Although a wide dither scheme is used to ensure a reasonable level of uniformity within the LSST FOV (see Figure 6 and Section 4.1 in Lee et al. 2024), the central region of 1° in radius is approximately 5% shallower in limiting flux than the average depth. Additionally, edge effects near the image boundaries where photometric noise is greater could masquerade as LAE overdensities. To address this, we apply a magnitude cut to the LAE sample when constructing the surface density map. Multiple realizations of ‘random’ density maps are also created by randomly selecting NB-detected sources (*without* any significant narrowband excess), and overdensity regions flagged in these maps are visually inspected. We find that the overdensities seen in the random maps do not significantly overlap with the regions where real protoclusters are detected, demonstrating that our detected

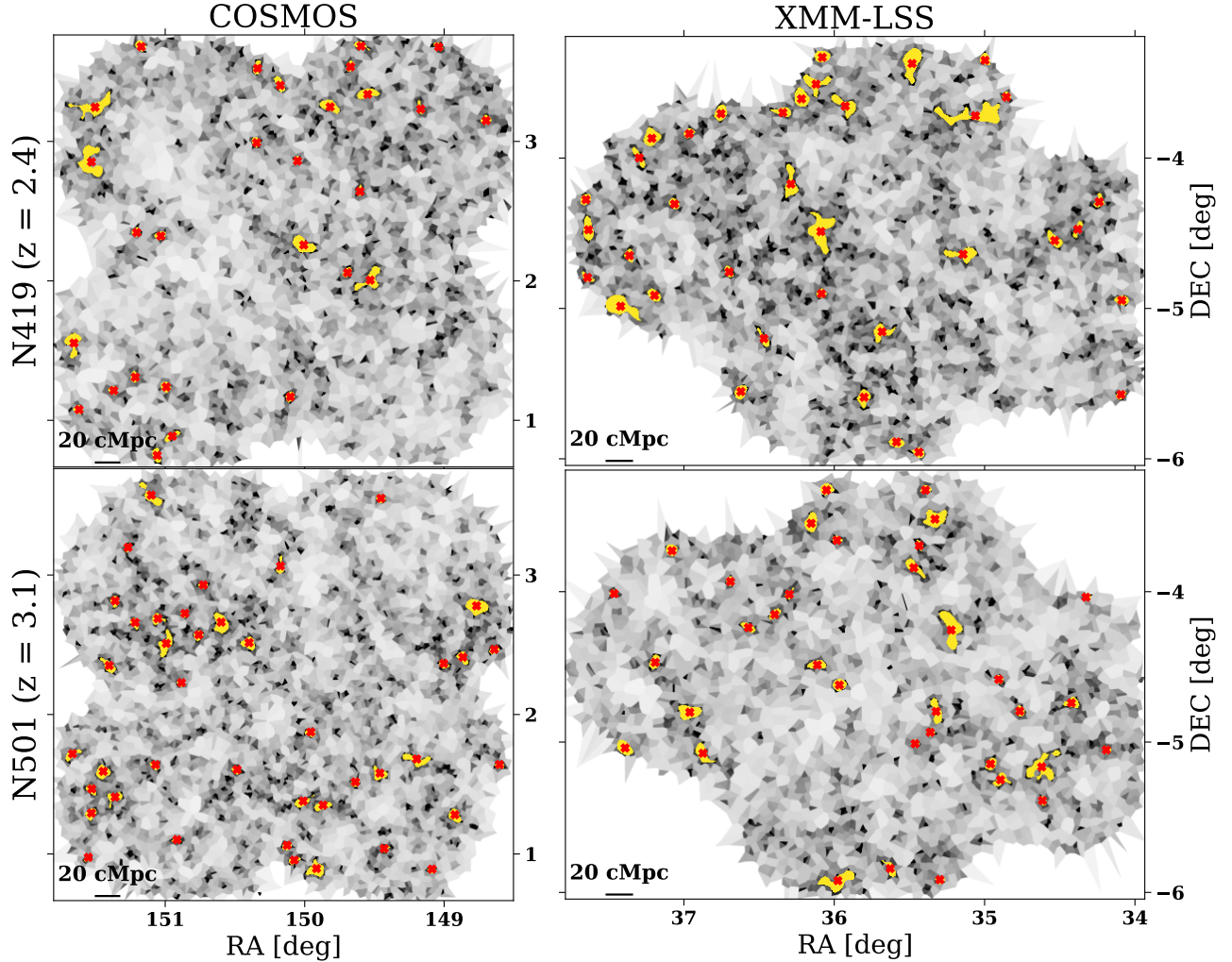


Figure 1. Protocluster candidates (yellow swaths) selected with our 4 field/filter combinations, overlaid on the Voronoi Tessellation-based LAE surface density maps. The shape of the density maps is a result of the arrangement of the four Deep HSC-SSP pointings in each field. The geometric centers of each protocluster are indicated by red crosses. The density threshold and minimum used to select these objects are given in the text.

protoclusters are unlikely to arise from noise fluctuations.

Figure 1 shows the locations of ODIN protoclusters as yellow swaths, with red crosses marking each protocluster’s geometric center. The final count of protoclusters in each field is provided in Table 1. The effective volume, V_{eff} , is calculated by converting the filter transmission curve into the redshift selection function. For comparison, the table also includes data from the protocluster sample used for clustering measurements in Toshikawa et al. (2018). Their sample, based on Lyman break galaxy (LBG) overdensities, features a much wider redshift selection function and covers an area approximately ten times larger than the ODIN sample. Table 1 shows that the number density of LBG-detected protoclusters is about 50 times lower than that of ODIN protoclus-

ters, suggesting that the LBG sample may trace rarer, more massive systems (see later).

In our earlier work (Ramakrishnan et al. 2024), we utilized data from IllustrisTNG, a suite of cosmological hydrodynamical simulations, to better understand the selection efficiency of ODIN protoclusters and to calibrate estimates of their descendant masses based on the level and angular extent of the LAE overdensity (δ_{LAE} and A). We created mock ODIN volumes from the $z = 3$ snapshot, centered on cosmic structures selected by their present-day mass. In doing so, we closely match the ODIN survey parameters including the line-of-sight thickness and the surface density of galaxies. For the latter, we randomly selected a subset of galaxies within a specific mass range to approximately match the observed clustering strength of LAEs (e.g., White et al. 2024). The mock data were then pro-

Table 1. Key parameters of large protocluster samples

Redshift	Field	Effective area	V_{eff}	NB depth ^a	N_g ^b	N_p ^c	n_p
		[deg ²]	[10 ⁶ cMpc ³]				[10 ⁻⁶ cMpc ⁻³]
2.45 ± 0.03 (ODIN)	COSMOS	7.3	4.6	25.37	6,441	28	6.1
	XMM-LSS	6.6	4.2	25.25	5,614	36	8.6
	Total	13.9	8.8		12,055	64	7.3
3.12 ± 0.03 (ODIN)	COSMOS	7.3	5.8	25.37	6,069	41	7.0
	XMM-LSS	6.6	5.2	25.47	3,928	35	6.6
	Total	13.9	11.0		9,997	76	6.9
3.8 ± 0.45 ^d	HSC-SSP Wide	121	1,510		366,690 ^e	216	0.14

^aMedian 5σ depth measured in a $2''$ diameter circular aperture

^bNumber of LAEs (see Firestone et al. 2024)

^cNumber of protocluster candidates (see Ramakrishnan et al. 2024)

^dKey numbers of the protocluster search conducted by Toshikawa et al. (2018) using LBGs as tracers

^eFrom Ono et al. (2018)

jected onto the XY, YZ, or XZ planes to create multiple sky images where we applied the protocluster detection criteria. For protoclusters with descendant masses of $M_{z=0} \gtrsim 2 \times 10^{14} M_{\odot}$, the recovery rate is $\approx 60\%$. Non-detection of about 40% occurs because, along some sightlines, TNG structures did not satisfy both criteria for the detection. Using the mass calibration, we find that the real ODIN protoclusters have a median descendant mass of $M_{z=0} \sim 10^{14.5} M_{\odot}$.

3. PROTOCLUSTER CROSS-CORRELATION MEASUREMENTS

The two-point correlation function (CF) is a straightforward method for measuring the clustering strength of a set of points. When applied to the positions of astronomical sources, the CF measure can be compared with the analytical or numerical models for the clustering of dark matter halos (e.g., Mo & White 1996), thereby providing insight into the properties of cosmic structures hosting them (e.g., Zehavi et al. 2004; Lee et al. 2006; Harikane et al. 2022). Similarly, the presence or absence of an evolutionary connection between two samples observed at different cosmic epochs can be established based on the CF, as the redshift evolution of halo clustering is known.

Because protoclusters are unvirialized structures, they are composed of multiple dark matter halos. The canonical theory of hierarchical structure formation dictates that all halos will merge with *the most massive halo within the protocluster* and become substructures within the dynamical timescale. In this context, the clustering

measurements at scales larger than the size of a protocluster probe the properties of these most massive halos, though for brevity, we will refer to quantities such as ‘protocluster bias’ in the following discussion. It is worth stating that, in the subsequent sections, we focus on the clustering of these parent halos and their redshift evolution, and not on internal clustering within a given protocluster structure.

3.1. Protocluster-LAE cross-correlation function

The most direct method for estimating the bias and mass of the most massive dark matter halos within the protoclusters is to measure the two-point auto-correlation function, as done by Toshikawa et al. (2018). However, our sample at each redshift is about one-third the size of theirs, leading to significant uncertainties in the auto-correlation function measurement. Instead, we opt to measure the cross-correlation function (CCF) between protoclusters and LAEs. Because the clustering properties of LAEs are well understood both in general (e.g., Kovač et al. 2007; Guaita et al. 2010; Lee et al. 2014) and for our samples (White et al. 2024, D. Herrera et al., in prep), this approach helps reduce measurement uncertainties, provided that certain assumptions hold (discussed later). As the ODIN survey nears completion, full auto-correlation function measurements will be presented in a future paper.

Using the Landy & Szalay (1993) estimator, we calculate the two-point protocluster-LAE cross-correlation

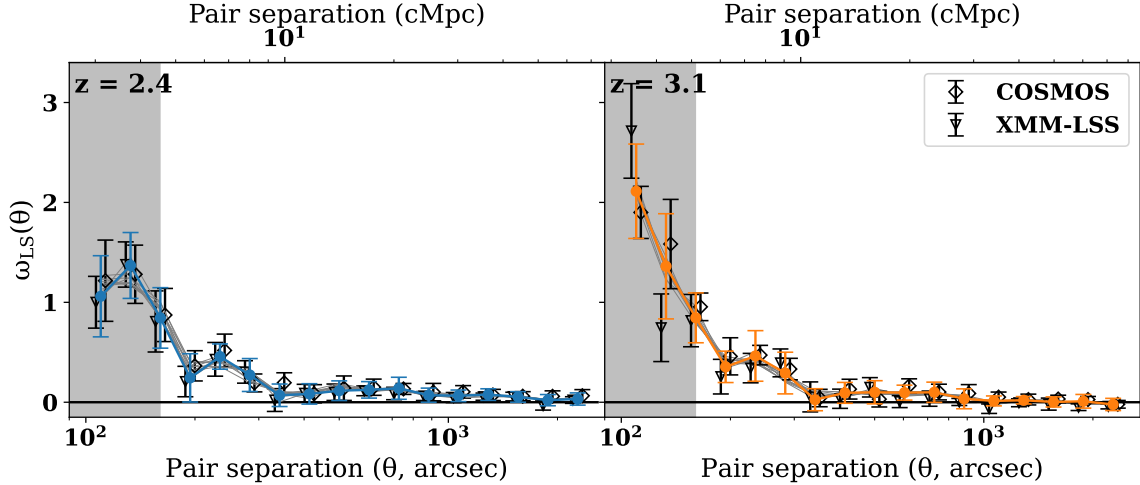


Figure 2. The cross-correlation function measurements are shown as a function of angular separation for $z = 2.4$ (left) and $z = 3.1$ (right), with the corresponding projected comoving separations displayed on the top axes. In each panel, the combined CCF is represented by color-filled circles and thick solid lines of the same color, while the individual measurements for the COSMOS and XMM-LSS fields are shown as black diamonds and downward triangles, respectively (offset slightly for clarity). Thin grey lines show the combined measurements using 10 random catalogs. The grey-shaded regions mark the median angular size of the ODIN protoclusters. A strong signal is detected at both redshift ranges.

function, $\omega_{\text{LS}}(\theta)$:

$$\omega_{\text{LS}}(\theta) = \frac{D_p D_g(\theta) - D_p R_g(\theta) - D_g R_p(\theta) + R_p R_g(\theta)}{R_g R_p(\theta)} \quad (1)$$

where $D_p D_g(\theta)$ is the number of protocluster-LAE pairs at angular separation of θ , with ‘p’ and ‘g’ denoting protoclusters and LAEs, respectively. $R_p R_g(\theta)$ is the analogous quantity for random pairs, and $D_p R_g(\theta)$ and $D_g R_p(\theta)$ are the number of random-source cross pairs. Logarithmic binning of the angular separations is chosen to ensure adequate sampling at both small- and large scales.

The position of each protocluster is shown as red crosses in Figure 1, overlaid on the LAE density map for each field. As described in Ramakrishnan et al. (2024), the local LAE density is measured and converted into a pixelated map with an angular resolution of $3''6$. A source detection algorithm is applied to this map to identify protoclusters and flag the pixels belonging to each structure. The position of each protocluster is defined as its geometric center, calculated as the geometric mean of all the associated pixels. Our main results remain consistent even if we use the pixel with the peak LAE density as the protocluster center.

To construct a random galaxy catalog (R_g), we select 20,000 sources with a signal-to-noise ratio greater than 5 from the narrow-band catalog such that their magnitude distribution matches the LAEs. This approach allows us to account for small depth variations that might affect our LAE selection by applying the same selection

effect to our random sources. Ten independent random catalogs are created for use. As for protocluster randoms (R_p), we generate 20,000 random points within the field, as the protocluster distribution only depends on the relative LAE *overdensity* and thus is insensitive to the survey depth. The same star masks used for our LAE sample are applied to both protoclusters and our random catalogs.

Each pair count in Equation 1 is made separately in the two fields and then combined as:

$$X_p X_g(\theta_j) = \frac{\sum_i X_{p,i} X_{g,i}(\theta_j)}{\sum_i \sum_k X_{p,i} X_{g,i}(\theta_k)} \quad (2)$$

where X is either D (data) or R (random), i refers to the i th field, and j or k indexes the angular bins. The covariance matrix, \mathcal{C} , for the CCF is computed using jackknife sampling by dividing the samples *in each field* into 15 subsamples and repeating the measurement 15 times, each time leaving out one subsample. \mathcal{C} has the dimension of $N_\theta \times N_\theta$ where N_θ is the number of angular bins in our CCF measures. The choice of 15 subsamples was determined by varying the number and identifying the minimum number at which the covariance matrix converged.

The resulting CCFs at both redshifts are shown in Figure 2 where the same measures for the COSMOS and XMM-LSS fields are also shown. In each case, the error bars represent the square root of the diagonal of the covariance matrix. For both redshift samples, the individual measures are consistent with the combined function within the uncertainties.

3.2. Protocluster bias

The bias b_X determines the scaling between the protocluster-LAE CCF, ω_X , and matter correlation function, ω_m , as:

$$\omega_X(\theta) = b_X^2 \omega_m(\theta) \quad (3)$$

where the former is related to our observational measure through the integral constraint (\mathcal{IC}), which accounts for the loss of power at scales larger than our survey fields and thus depends on the size of the field and the galaxy and protocluster power spectrum. The two are related as:

$$1 + \omega_{\text{LS}}(\theta) = \frac{1 + \omega_X(\theta)}{1 + \mathcal{IC}} \quad (4)$$

Following the prescription given by [Adelberger et al. \(2005\)](#) (also see, [Infante 1994](#); [Roche & Eales 1999](#)), we estimate \mathcal{IC} as,

$$\mathcal{IC} = \frac{\sum_j R_g R_p(\theta_j) \omega_X(\theta_j)}{\sum_j R_g R_p(\theta_j)} = b_X^2 \frac{\sum_j R_g R_p(\theta_j) \omega_m(\theta_j)}{\sum_j R_g R_p(\theta_j)} \quad (5)$$

By combining Equations 3, 4 and 5, we can write down $\omega_{\text{LS}}(\theta)$ in terms of all other quantities as:

$$\omega_{\text{LS}}(\theta) = b_X^2 \frac{\omega_m(\theta) - [\sum_j R_g R_p(\theta_j) \omega_m(\theta_j) / \sum_j R_g R_p(\theta_j)]}{1 + b_X^2 [\sum_j R_g R_p(\theta_j) \omega_m(\theta_j) / \sum_j R_g R_p(\theta_j)]} \quad (6)$$

We calculate b_X using this equation where $\omega_m(\theta)$ is obtained from the angular matter power spectrum using the Core Cosmology Library (CCL, [Chisari et al. 2019](#)).

The uncertainty in b_X is estimated by generating 5,000 realizations of the CCF according to a multivariate normal distribution of the form $\exp[-(x_i - \mu_i) \mathcal{C}_{ij}^{-1} (x_j - \mu_j)]$. Here, x_i is the value of the perturbed CCF in the angular bin θ_i and μ_i and \mathcal{C}_{ij} are the measured CCF, $\omega_{\text{LS}}(\theta_i)$, and its covariance, respectively. Each realization is fit using Equation 6 to determine the corresponding b_X value. For the fit, we only include the angular bins with $\theta \geq 160''$, which corresponds to a projected separation of 4.6 (5.0) cMpc at $z = 2.4$ (3.1), roughly matching the typical size of the ODIN protoclusters¹. At scales smaller than a protocluster, the CCF is expected to deviate from a power-law due to LAEs residing in the same protocluster (the ‘‘one-halo’’ term). As illustrated in Figure 3, the best-fit power-laws to our data

¹ The size is computed as the median effective radius as $\sqrt{A/\pi}$ where A is the transverse area rising above the adopted detection threshold δ_{LAE} for a given protocluster. See Section 2 for more details.

lie significantly below the measured values for angular separations of $\theta \lesssim 160''$. The exclusion of the small-scale clustering from the fitting means that our results are insensitive to the uncertainty in protocluster centers. In Table 2, we report the best-fit b_X values where the upper and lower limits indicate the 16th and 84th percentile, respectively.

The CCF bias, b_X , is the geometric mean of the protocluster bias (b_p) and LAE bias (b_g). The LAE bias is known from the clustering measurements of ODIN LAEs ([White et al. 2024](#), [D. Herrera et al., in prep](#)), which yield in 1.7 ± 0.2 at $z = 2.4$ and 2.0 ± 0.2 at $z = 3.1$. Using this, we can now estimate the protocluster bias as $b_p = b_X^2 / b_g$. The results are summarized in Table 2 where the uncertainties in both b_X and b_g are propagated into those in b_p . The inferred protocluster bias is $b_p \approx 6 - 7$, much higher than any known galaxy population. Previous studies showed that LBGs at similar redshift typically have $b \sim 2 - 3$ ([Lee et al. 2006](#); [Hildebrandt et al. 2009](#); [Harikane et al. 2022](#)) while more UV-faint LAEs tend to have even lower biases, $b \sim 1.5 - 2.0$ (e.g., [Guaita et al. 2010](#); [White et al. 2024](#)). The high bias values imply that ODIN-selected structures correspond to more massive dark matter halos than these galaxy populations.

3.3. Protocluster correlation length

If the real-space correlation function follows a power law, $\xi(r) = (r/r_0)^{-\gamma}$, where r_0 is the correlation length, the corresponding angular correlation function, $\omega(\theta)$, takes the form $A_\omega \theta^{-\beta}$ and is related to $\xi(r)$ through the [Limber \(1953\)](#) equation:

$$A_\omega = C r_{0,X}^\gamma \int_0^\infty F(z) D_\theta^{1-\gamma}(z) N(z)^2 g(z) dz, \quad (7)$$

where $\gamma = 1 + \beta$, $F(z)$ describes the redshift dependence of $\xi(r)$, $D_\theta(z)$ is the angular diameter distance at redshift z , $N(z)$ is the redshift selection function for the galaxy sample, and

$$g(z) = \frac{H_0}{c} \left[(1+z)^2 (1 + \Omega_M z + \Omega_\Lambda [(1+z)^{-2} - 1])^{\frac{1}{2}} \right]. \quad (8)$$

Here, $C = \sqrt{\pi} \Gamma((\gamma - 1)/2) / \Gamma(\gamma/2)$. Given the narrow transmission widths of our filters (corresponding to a line-of-sight thickness of 60–70 cMpc), it is reasonable to assume $F(z) = 1$. We convert the total throughput of each filter to obtain $N(z)$ (see Figure 1 of [Lee et al. 2024](#)).

Under the power-law assumption, we estimate the correlation lengths as follows. As before, we generate 5,000

Table 2. Biases, correlation lengths, and halo masses of ODIN protoclusters

Redshift	b_X	b_g^a	b_p^b	$r_{0,X}$	$r_{0,g}^a$	$r_{0,p}^b$	$\log(M_{\min}/M_\odot)$	$\log \langle M \rangle / M_\odot$	n_h
		(fixed)		(cMpc)	(fixed, cMpc)	(cMpc)			(10^{-6} cMpc $^{-3}$)
2.4	$3.36^{+0.21}_{-0.23}$	1.7 ± 0.2	$6.6^{+1.3}_{-1.1}$	$10.10^{+0.82}_{-0.84}$	4.3 ± 0.3	$23.7^{+4.2}_{-4.3}$	$13.31^{+0.24}_{-0.26}$	$13.53^{+0.21}_{-0.24}$	$2.8^{+9.5}_{-2.2}$
3.1	$3.47^{+0.33}_{-0.33}$	2.0 ± 0.2	$6.1^{+1.3}_{-1.3}$	$8.78^{+1.01}_{-0.99}$	4.3 ± 0.3	$17.9^{+4.3}_{-4.2}$	$12.76^{+0.32}_{-0.39}$	$12.96^{+0.28}_{-0.33}$	$15.5^{+8.3}_{-1.3}$

^a Measured LAE bias from White et al. (2024)

^b Uncertainties are estimated by propagating the errors on input quantities assuming that they are uncorrelated.

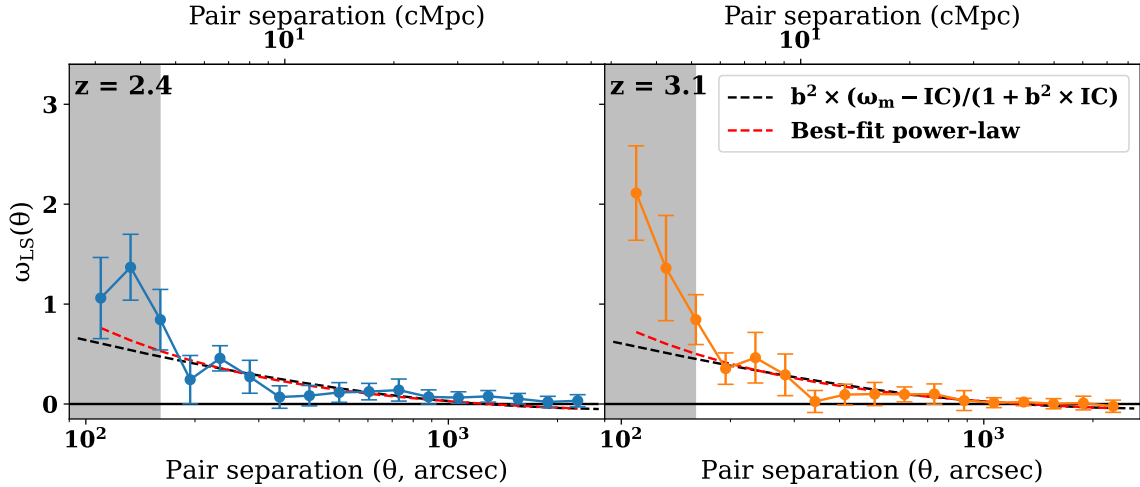


Figure 3. Cross-correlation functions together with median bias values (black dashed lines) which give the best fit of Equation 6 to our observed cross-correlation functions. Red dashed lines show the best-fit power-law model with integral constraint.

realizations of the CCF from our ω_{LS} measurements. Using Equations 4 and 5, we determine the best-fit A_ω . The β value is fixed to 0.8 to match the result from White et al. (2024); it is also consistent with the power-law slopes found or assumed by existing studies. The correlation length, $r_{0,X}$, is calculated using Equation 7. Re-fitting the CCF after fixing β to 0.6 or 1.0 yield functionally identical results for the correlation length, which is unsurprising given that β and A_ω are strongly correlated. The best-fit power-law with the median value of A_ω in Figure 3 together with our CCF measures.

If the real-space correlation functions for both protoclusters and LAEs share the same power-law slope, γ , it can be shown that their correlation lengths are related through:

$$r_{0,p} = \frac{r_{0,X}^2}{r_{0,g}} \quad (9)$$

We adopt $r_{0,g} = 4.3 \pm 0.3$ cMpc for both redshift samples as reported by White et al. (2024). Table 2 lists the best-fit $r_{0,X}$ and $r_{0,p}$ values.

As expected from the large bias values we obtained earlier, the inferred correlation lengths for ODIN protoclusters are large, $r_{0,p} = 18 - 24$ cMpc. For comparison, for flux-limited ($\mathcal{R} \leq 25.5$) LBG samples at $z \sim 2.2$ and 2.9, Adelberger et al. (2005) reported $r_0 = 4.2 \pm 0.5$ and $4.0 \pm 0.6 h^{-1}$ cMpc, respectively. For more UV-luminous LBGs ($r \leq 24.5$) at $z \sim 3$, Hildebrandt et al. (2009) found $r_0 = 5.9 \pm 0.4 h^{-1}$ cMpc, in agreement with luminosity-dependent clustering strength (e.g., Giavalisco & Dickinson 2001; Lee et al. 2006; Harikane et al. 2022). Finally, we note that, at $z \sim 3.8$, Toshikawa et al. (2018) estimated the correlation length for their LBG-selected protocluster candidates to be $35.7^{+4.6}_{-5.5} h^{-1}$ cMpc, i.e., much larger than our value. In Section 4.1, we discuss this difference in the context of redshift evolution of the abundance and clustering properties of halos.

4. DISCUSSION

4.1. Halo mass and abundance of ODIN protoclusters

Both the space density and clustering strength of halos strongly depend on halo mass, with more massive halos being rarer and more biased tracers of the underlying matter distribution compared to less massive ones. In this section, we use the analytic framework developed by Sheth & Tormen (1999) and Mo & White (2002) to analyze our data and infer the properties of the halos hosting ODIN protoclusters. All calculations are performed using the CCL library routines.

If the minimum mass of the halos associated with an ODIN protocluster is M_{\min} , the average bias of the sample can be expressed as:

$$\langle b_h \rangle = \frac{\int_{M_{\min}}^{\infty} b(M)n(M)dM}{\int_{M_{\min}}^{\infty} n(M)dM} \quad (10)$$

where $b(M)$ is the bias of halos with mass M , and $n(M)$ is the halo mass function, following the Sheth & Tormen (1999) model. The best-fit M_{\min} value is determined by setting $b_p = \langle b_h \rangle$, where b_p is the protocluster bias obtained in Section 3.2. Once M_{\min} is known, the mean halo mass $\langle M \rangle$ is calculated as:

$$\langle M \rangle = \frac{\int_{M_{\min}}^{\infty} Mn(M)dM}{\int_{M_{\min}}^{\infty} n(M)dM}. \quad (11)$$

The values of M_{\min} and $\langle M \rangle$, listed in Table 2, suggest that the most massive halo within the ODIN protoclusters has a typical mass of $\langle M \rangle \approx 10^{13}M_{\odot}$ at the time of observation. The similarity between the M_{\min} and $\langle M \rangle$ values is expected, as the steep slope of the halo mass function means that the number of halos in a sample is dominated by those close to the cut-off mass.

Finally, we calculate the number density of halos whose clustering matches the observed value by integrating the halo mass function above M_{\min} :

$$n_h = \int_{M_{\min}}^{\infty} n(M)dM \quad (12)$$

By comparing this to the number density of protoclusters, n_p , the ratio n_p/n_h gives an estimate of the completeness of the protocluster selection. For example, if only 50% of halos above a given mass threshold are observationally detected as a protocluster, both samples would have the same clustering strength, but $n_p/n_h = 0.5$.

While $n_p/n_h > 1$ is theoretically unphysical, sample contamination or uncertainties in the measured protocluster bias could lead to ratios exceeding unity. As structures observed well before virialization, protoclusters are expected to be extended and have irregular morphologies. The sky distribution of galaxies in several well-studied protoclusters supports this view (e.g.,

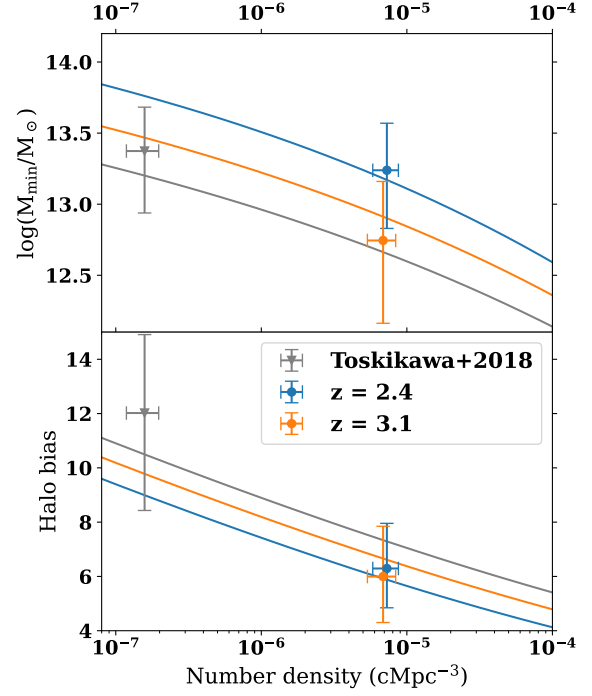


Figure 4. Color lines show the expected relationship between M_{\min} (top) or $\langle b_h \rangle$ (bottom) and the number density of halos above the threshold (n_h) at a redshift of $z = 2.4$ (blue), 3.1 (orange), and 3.8 (grey), representing the LAE-selected ODIN protoclusters and LBG-selected sample from Toshikawa et al. (2018), respectively. The data points show the protocluster number density n_p and the M_{\min} and b_p values inferred from clustering measurements.

Hayashino et al. 2004; Dey et al. 2016; Cucciati et al. 2018). Depending on the viewing angle, a single structure may be fragmented into more than one structure, leading to an overestimation of n_p . Conversely, the opposite effect could also occur, where n_p is underestimated.

Using the data from Tables 1 and 2, we find $n_p/n_h = 2.7_{-2.3}^{+18.6}$ at $z = 2.4$ and $0.44_{-0.40}^{+4.6}$ at $z = 3.1$. The latter value is consistent with an independent estimate from mock datasets based on IllustrisTNG, as described in Section 2 (also see Ramakrishnan et al. 2024, for more detail). Overall, we observe a high completeness (50–100%) for ODIN protocluster selection. In contrast, the protoclusters identified by Toshikawa et al. (2018) show a significantly higher ratio of $n_p/n_h \approx 5.3$.

Our findings are visualized in Figure 4. In the top panel, the colored lines represent the expected relationship between M_{\min} and n_h for halos at the redshift of the ODIN protocluster sample and the Toshikawa et al. (2018) sample. Similarly, the lines in the bottom panel show the predicted $\langle b_h \rangle$ - n_h scaling relations. The data points correspond to the b_p or M_{\min} values inferred from

clustering measurements plotted against n_p . By requiring that the halo and protocluster samples have the same clustering strength (i.e., identical b_p or M_{\min} values), the completeness, represented by the ratio n_p/n_h , can be determined.

The protocluster correlation length and predicted halo mass in our sample are both lower than those reported by Toshikawa et al. (2018)— $51.7^{+4.4}_{-4.9}$ cMpc and $(3.4 \pm 0.7) \times 10^{13} M_{\odot}$ at $z \sim 3.8$ —suggesting that their sample likely contains more massive structures. Given the near-unity completeness of our sample, this difference is unlikely to stem from fundamental differences in how LBGs and LAEs trace cosmic structures. Instead, it is likely a selection effect. The redshift range for LBG selection is much broader (with a half-width-at-half-maximum of $\Delta z \approx 0.3 - 0.4$) than for LAE-based selections like ODIN ($\Delta z \sim 0.03$), making LBG samples more susceptible to projection effects from foreground and background interlopers. As a result, the cosmic structures identified as significant LBG overdensities are likely to be more massive than those selected based on LAE overdensities.

4.2. Projected evolution and likely descendants

What kinds of structures will ODIN protoclusters evolve into by the present-day universe? In this section, we explore this question by examining the cosmic evolution of dark matter halos. The simplest method is to trace halos with a fixed number density across cosmic time, assuming that each parent halo associated with a protocluster at high redshift will evolve into a distinct halo hosting a galaxy cluster at $z = 0$. Starting from the protocluster number density n_p , we find that the mean descendant mass is $\langle M_{z=0} \rangle \sim 3.5 \times 10^{14} M_{\odot}$ and $3.6 \times 10^{14} M_{\odot}$ at $z = 2.4$ and 3.1 , respectively. Possible caveats of this approach include selection bias and completeness.

A similar approach, but using the n_h value, should be more robust against counting errors, as the estimate is based on clustering. The inferred descendant masses are consistent within uncertainties, with $\langle M \rangle = 5.5^{+7.1}_{-3.6} \times 10^{14} M_{\odot}$ and $2.3^{+4.9}_{-1.8} \times 10^{14} M_{\odot}$ at $z = 2.4$ and 3.1 , respectively. ODIN protoclusters are expected to evolve into intermediate-mass clusters, similar to the Virgo cluster. The clustering-based masses are consistent with a heuristic estimate presented in Ramakrishnan et al. (2024).

Figure 5 shows the redshift evolution of $\langle M \rangle$ at several fixed number densities. The dashed lines represent the mass growth history of a halo, assuming it does not merge with another halo of comparable mass. Overlaid on the figure are observational measurements

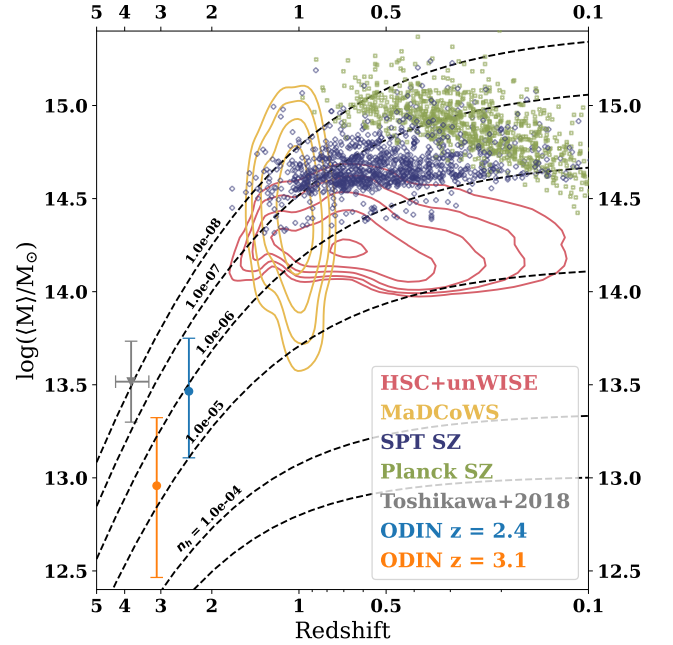


Figure 5. Mean halo mass of the ODIN protoclusters compared to various cluster samples at low redshift (adapted from Albers & Noble 2022). Black dashed lines show the expected evolution of halo mass with redshift assuming a constant number density. An average ODIN protocluster will evolve into structures with masses comparable to high-redshift clusters identified through photometric selection.

from recent cluster surveys compiled by Albers & Noble (2022). These include clusters identified via the Sunyaev-Zeldovich (SZ) effect by *Planck* (Planck Collaboration et al. 2014) and the South Pole Telescope (Bleem et al. 2015, 2020; Huang et al. 2020), as well as clusters detected as high galaxy overdensities in the Massive and Distant Clusters of WISE Survey (MaDCoWS: Gonzalez et al. 2019) and a photometric redshift catalog based on Hyper-SuprimeCam (HSC) and unWISE data (Wen & Han 2021).

The figure illustrates that an average ODIN protocluster will evolve into structures with masses comparable to high-redshift ($z = 0.7 - 1.0$) clusters identified through photometric selection (HSC+unWISE in Figure 5). The top 5–15% of ODIN protoclusters² will evolve into clusters with masses exceeding $10^{15} M_{\odot}$, significantly overlapping with MaDCoWS clusters at $z \approx 1$ and SZ-selected clusters at lower redshift. In contrast,

² This assumes that the completeness of ODIN protocluster detection is independent of descendant mass. However, in Ramakrishnan et al. (2024), we demonstrate that more massive protoclusters are more likely to be detected. In a simple model where the completeness is 50% below and 100% above $M_{z=0} = 10^{15} M_{\odot}$, our estimate changes to 10-30%.

the protoclusters studied by Toshikawa et al. (2018) are expected to evolve into some of the rarest and most massive clusters, far exceeding the mass of the Coma cluster. This is consistent with their much lower space density and higher minimum mass, even though they are observed at an earlier epoch ($z \approx 3.8$) compared to the ODIN protoclusters examined in this study (Figure 4).

Finally, we highlight that the two ODIN protocluster samples have similar descendant masses, suggesting that they are likely comparable structures observed at different stages in their evolution. As a result, the results from ODIN will not only provide valuable insight into the properties of massive structures but also will enable us to directly trace the evolutionary sequence of galaxies therein over cosmic time.

5. SUMMARY

We report strong clustering of protoclusters at $z = 2.4$ and 3.1 identified as significant LAE overdensities by the ODIN survey over a total area of $\approx 14 \text{ deg}^2$. Through cross-correlation function measurements, we infer the correlation length and halo bias of ODIN protoclusters. Both quantities are significantly higher than those typically observed for galaxy populations at these epochs, validating that ODIN protocluster selection indeed pinpoints the sites of the rarest, most massive halos. By comparing the protocluster number density to that of halos with similar clustering amplitude, we estimate the completeness of ODIN protocluster selection to be of the order of unity, consistent with an independent estimate from cosmological hydrodynamical simulations (Ramakrishnan et al. 2024).

At $z = 2.4$ and 3.1 , the mean masses of the halos hosting these protoclusters are $\log(M/M_\odot) = 13.53^{+0.21}_{-0.24}$ and $12.96^{+0.28}_{-0.33}$, respectively. The top 10–30% of ODIN protoclusters will evolve into the most massive clusters ($M_{z=0} \gtrsim 10^{15} M_\odot$), similar to SZ-selected clusters at low redshift, while the average ODIN protocluster is likely to become a more typical, lower-mass cluster detected by photometric surveys. The range of descendant masses for ODIN protoclusters is in good agreement with more

heuristic estimates based on the level and the angular extent of the LAE overdensity calibrated against cosmological simulations.

At both redshifts, the mean descendant masses ($M_{z=0} \approx 10^{14.0-14.5} M_\odot$) are comparable, indicating that these protoclusters represent similar cosmic structures observed at different epochs. This close evolutionary relationship between the two samples suggests that any observed redshift-dependent trends can be reasonably interpreted as redshift evolution. The final ODIN protocluster samples are expected to be several times larger than those presented in this work and will extend out to $z = 4.5$. ODIN will provide clean, well-calibrated samples of protoclusters that can be directly linked to lower-redshift systems, thereby elucidating the formation history of the present-day clusters of galaxies.

- 1 The authors acknowledge financial support from the
- 2 National Science Foundation under Grant Nos. AST-
- 3 2206705, AST-2408359, and AST-2206222, and from the
- 4 Ross-Lynn Purdue Research Foundations. This material
- 5 is based upon work supported by the National Science
- 6 Foundation Graduate Research Fellowship Program under
- 7 Grant No. DGE-2233066 to NF. J.L. is supported
- 8 by the National Research Foundation of Korea (NRF-
- 9 2021R1C1C2011626). H.S. acknowledges the support
- 10 of the National Research Foundation of Korea (NRF)
- 11 grant funded by the Korean government (MSIT) (No.
- 12 2022R1A4A3031306). The Institute for Gravitation and
- 13 the Cosmos is supported by the Eberly College of Sci-
- 14 ence and the Office of the Senior Vice President for Re-
- 15 search at the Pennsylvania State University. Based on
- 16 observations at Cerro Tololo Inter-American Observa-
- 17 tory, NSF's NOIRLab (Prop. ID 2020B-0201; PI: K.-S.
- 18 Lee), which is managed by the Association of Univer-
- 19 sities for Research in Astronomy under a cooperative
- 20 agreement with the National Science Foundation.

Facility: Blanco

Software: SExtractor (Bertin & Arnouts 1996), SEP (Barbary 2016), CCL (Chisari et al. 2019), Astropy (Astropy Collaboration et al. 2013, 2018, 2022)

REFERENCES

- Adelberger, K. L., Steidel, C. C., Pettini, M., et al. 2005, ApJ, 619, 697, doi: [10.1086/426580](https://doi.org/10.1086/426580)
- Aihara, H., Arimoto, N., Armstrong, R., et al. 2018a, PASJ, 70, S4, doi: [10.1093/pasj/psx066](https://doi.org/10.1093/pasj/psx066)
- Aihara, H., Armstrong, R., Bickerton, S., et al. 2018b, PASJ, 70, S8, doi: [10.1093/pasj/psx081](https://doi.org/10.1093/pasj/psx081)
- Alberty, S., & Noble, A. 2022, Universe, 8, 554, doi: [10.3390/universe8110554](https://doi.org/10.3390/universe8110554)
- Astropy Collaboration, Robitaille, T. P., Tollerud, E. J., et al. 2013, A&A, 558, A33, doi: [10.1051/0004-6361/201322068](https://doi.org/10.1051/0004-6361/201322068)

- Astropy Collaboration, Price-Whelan, A. M., Sipőcz, B. M., et al. 2018, *AJ*, 156, 123, doi: [10.3847/1538-3881/aabc4f](https://doi.org/10.3847/1538-3881/aabc4f)
- Astropy Collaboration, Price-Whelan, A. M., Lim, P. L., et al. 2022, *ApJ*, 935, 167, doi: [10.3847/1538-4357/ac7c74](https://doi.org/10.3847/1538-4357/ac7c74)
- Barbary, K. 2016, *The Journal of Open Source Software*, 1, 58, doi: [10.21105/joss.00058](https://doi.org/10.21105/joss.00058)
- Bertin, E., & Arnouts, S. 1996, *A&AS*, 117, 393, doi: [10.1051/aas:1996164](https://doi.org/10.1051/aas:1996164)
- Bleem, L. E., Stalder, B., de Haan, T., et al. 2015, *ApJS*, 216, 27, doi: [10.1088/0067-0049/216/2/27](https://doi.org/10.1088/0067-0049/216/2/27)
- Bleem, L. E., Bocquet, S., Stalder, B., et al. 2020, *ApJS*, 247, 25, doi: [10.3847/1538-4365/ab6993](https://doi.org/10.3847/1538-4365/ab6993)
- Casey, C. M., Cooray, A., Capak, P., et al. 2015, *ApJL*, 808, L33, doi: [10.1088/2041-8205/808/2/L33](https://doi.org/10.1088/2041-8205/808/2/L33)
- Chiang, Y.-K., Overzier, R., & Gebhardt, K. 2013, *ApJ*, 779, 127, doi: [10.1088/0004-637X/779/2/127](https://doi.org/10.1088/0004-637X/779/2/127)
- . 2014, *ApJL*, 782, L3, doi: [10.1088/2041-8205/782/1/L3](https://doi.org/10.1088/2041-8205/782/1/L3)
- Chisari, N. E., Alonso, D., Krause, E., et al. 2019, *ApJS*, 242, 2, doi: [10.3847/1538-4365/ab1658](https://doi.org/10.3847/1538-4365/ab1658)
- Coupon, J., Czakon, N., Bosch, J., et al. 2018, *PASJ*, 70, S7, doi: [10.1093/pasj/psx047](https://doi.org/10.1093/pasj/psx047)
- Cucciati, O., Lemaux, B. C., Zamorani, G., et al. 2018, *A&A*, 619, A49, doi: [10.1051/0004-6361/201833655](https://doi.org/10.1051/0004-6361/201833655)
- Dey, A., Lee, K.-S., Reddy, N., et al. 2016, *ApJ*, 823, 11, doi: [10.3847/0004-637X/823/1/11](https://doi.org/10.3847/0004-637X/823/1/11)
- Firestone, N. M., Gawiser, E., Ramakrishnan, V., et al. 2024, *ApJ*, 974, 217, doi: [10.3847/1538-4357/ad71c9](https://doi.org/10.3847/1538-4357/ad71c9)
- Gawiser, E., van Dokkum, P. G., Gronwall, C., et al. 2006, *ApJL*, 642, L13, doi: [10.1086/504467](https://doi.org/10.1086/504467)
- Gawiser, E., Francke, H., Lai, K., et al. 2007, *ApJ*, 671, 278, doi: [10.1086/522955](https://doi.org/10.1086/522955)
- Gialvalisco, M., & Dickinson, M. 2001, *ApJ*, 550, 177, doi: [10.1086/319715](https://doi.org/10.1086/319715)
- Gonzalez, A. H., Gettings, D. P., Brodwin, M., et al. 2019, *ApJS*, 240, 33, doi: [10.3847/1538-4365/aafad2](https://doi.org/10.3847/1538-4365/aafad2)
- Guaita, L., Gawiser, E., Padilla, N., et al. 2010, *ApJ*, 714, 255, doi: [10.1088/0004-637X/714/1/255](https://doi.org/10.1088/0004-637X/714/1/255)
- Harikane, Y., Ouchi, M., Ono, Y., et al. 2019, *ApJ*, 883, 142, doi: [10.3847/1538-4357/ab2cd5](https://doi.org/10.3847/1538-4357/ab2cd5)
- Harikane, Y., Ono, Y., Ouchi, M., et al. 2022, *ApJS*, 259, 20, doi: [10.3847/1538-4365/ac3dfc](https://doi.org/10.3847/1538-4365/ac3dfc)
- Hayashino, T., Matsuda, Y., Tamura, H., et al. 2004, *AJ*, 128, 2073, doi: [10.1086/424935](https://doi.org/10.1086/424935)
- Higuchi, R., Ouchi, M., Ono, Y., et al. 2019, *ApJ*, 879, 28, doi: [10.3847/1538-4357/ab2192](https://doi.org/10.3847/1538-4357/ab2192)
- Hildebrandt, H., Pielorz, J., Erben, T., et al. 2009, *A&A*, 498, 725, doi: [10.1051/0004-6361/200811042](https://doi.org/10.1051/0004-6361/200811042)
- Hong, S., Dey, A., Lee, K.-S., et al. 2019, *MNRAS*, 483, 3950, doi: [10.1093/mnras/sty3219](https://doi.org/10.1093/mnras/sty3219)
- Huang, N., Bleem, L. E., Stalder, B., et al. 2020, *AJ*, 159, 110, doi: [10.3847/1538-3881/ab6a96](https://doi.org/10.3847/1538-3881/ab6a96)
- Infante, L. 1994, *A&A*, 282, 353
- Ito, K., Tanaka, M., Valentino, F., et al. 2023, *ApJL*, 945, L9, doi: [10.3847/2041-8213/acb49b](https://doi.org/10.3847/2041-8213/acb49b)
- Jin, S., Sillassen, N. B., Magdis, G. E., et al. 2024, *A&A*, 683, L4, doi: [10.1051/0004-6361/202348540](https://doi.org/10.1051/0004-6361/202348540)
- Kovač, K., Somerville, R. S., Rhoads, J. E., Malhotra, S., & Wang, J. 2007, *ApJ*, 668, 15, doi: [10.1086/520668](https://doi.org/10.1086/520668)
- Kusakabe, H., Shimasaku, K., Ouchi, M., et al. 2018, *PASJ*, 70, 4, doi: [10.1093/pasj/psx148](https://doi.org/10.1093/pasj/psx148)
- Landy, S. D., & Szalay, A. S. 1993, *ApJ*, 412, 64, doi: [10.1086/172900](https://doi.org/10.1086/172900)
- Lee, K.-S., Dey, A., Hong, S., et al. 2014, *ApJ*, 796, 126, doi: [10.1088/0004-637X/796/2/126](https://doi.org/10.1088/0004-637X/796/2/126)
- Lee, K.-S., Gialvalisco, M., Gnedin, O. Y., et al. 2006, *ApJ*, 642, 63, doi: [10.1086/500387](https://doi.org/10.1086/500387)
- Lee, K.-S., Gawiser, E., Park, C., et al. 2024, *ApJ*, 962, 36, doi: [10.3847/1538-4357/ad165e](https://doi.org/10.3847/1538-4357/ad165e)
- Limber, D. N. 1953, *ApJ*, 117, 134, doi: [10.1086/145672](https://doi.org/10.1086/145672)
- Mo, H. J., & White, S. D. M. 1996, *MNRAS*, 282, 347, doi: [10.1093/mnras/282.2.347](https://doi.org/10.1093/mnras/282.2.347)
- . 2002, *MNRAS*, 336, 112, doi: [10.1046/j.1365-8711.2002.05723.x](https://doi.org/10.1046/j.1365-8711.2002.05723.x)
- Ono, Y., Ouchi, M., Harikane, Y., et al. 2018, *PASJ*, 70, S10, doi: [10.1093/pasj/psx103](https://doi.org/10.1093/pasj/psx103)
- Oteo, I., Ivison, R. J., Dunne, L., et al. 2018, *ApJ*, 856, 72, doi: [10.3847/1538-4357/aaa1f1](https://doi.org/10.3847/1538-4357/aaa1f1)
- Overzier, R. A. 2016, *A&A Rv*, 24, 14, doi: [10.1007/s00159-016-0100-3](https://doi.org/10.1007/s00159-016-0100-3)
- Peng, Y.-j., Lilly, S. J., Kovač, K., et al. 2010, *ApJ*, 721, 193, doi: [10.1088/0004-637X/721/1/193](https://doi.org/10.1088/0004-637X/721/1/193)
- Planck Collaboration, Ade, P. A. R., Aghanim, N., et al. 2014, *A&A*, 571, A29, doi: [10.1051/0004-6361/201321523](https://doi.org/10.1051/0004-6361/201321523)
- . 2016, *A&A*, 594, A27, doi: [10.1051/0004-6361/201525823](https://doi.org/10.1051/0004-6361/201525823)
- Quadri, R. F., Williams, R. J., Franx, M., & Hildebrandt, H. 2012, *ApJ*, 744, 88, doi: [10.1088/0004-637X/744/2/88](https://doi.org/10.1088/0004-637X/744/2/88)
- Ramakrishnan, V., Lee, K.-S., Artale, M. C., et al. 2024, *arXiv e-prints*, arXiv:2406.08645, doi: [10.48550/arXiv.2406.08645](https://doi.org/10.48550/arXiv.2406.08645)
- Roche, N., & Eales, S. A. 1999, *MNRAS*, 307, 703, doi: [10.1046/j.1365-8711.1999.02652.x](https://doi.org/10.1046/j.1365-8711.1999.02652.x)
- Sheth, R. K., & Tormen, G. 1999, *MNRAS*, 308, 119, doi: [10.1046/j.1365-8711.1999.02692.x](https://doi.org/10.1046/j.1365-8711.1999.02692.x)
- Staab, P., Lemaux, B. C., Forrest, B., et al. 2024, *MNRAS*, 528, 6934, doi: [10.1093/mnras/stae301](https://doi.org/10.1093/mnras/stae301)
- Toshikawa, J., Kashikawa, N., Overzier, R., et al. 2016, *ApJ*, 826, 114, doi: [10.3847/0004-637X/826/2/114](https://doi.org/10.3847/0004-637X/826/2/114)

Toshikawa, J., Uchiyama, H., Kashikawa, N., et al. 2018, PASJ, 70, S12, doi: [10.1093/pasj/psx102](https://doi.org/10.1093/pasj/psx102)

Wen, Z. L., & Han, J. L. 2021, MNRAS, 500, 1003, doi: [10.1093/mnras/staa3308](https://doi.org/10.1093/mnras/staa3308)

White, M., Raichoor, A., Dey, A., et al. 2024, arXiv e-prints, arXiv:2406.01803, doi: [10.48550/arXiv.2406.01803](https://doi.org/10.48550/arXiv.2406.01803)

Zehavi, I., Weinberg, D. H., Zheng, Z., et al. 2004, ApJ,

608, 16, doi: [10.1086/386535](https://doi.org/10.1086/386535)